Thermal Stability and Irradiation Response of Nanocrystalline CoCrCuFeNi High-entropy Alloy

Yanwen Zhang[1,2*], Matheus A. Tunes[3], Miguel L. Crespillo[2], Fuxiang Zhang[1], Walker L. Boldman[2], Philip D. Rack[2,4], Li Jiang[5], Chen Xu[2], Graeme Greaves[3], Stephen E. Donnelly[3], Lumin Wang[5], and William J. Weber[2,1]

[1] *Materials Science and Technology Division, Oak Ridge National Laboratory, Oak Ridge, TN 37831, United States*
[2] *Department of Materials Science and Engineering, University of Tennessee, Knoxville, TN 37996, USA*
[3] *School of Computing and Engineering, University of Huddersfield, Huddersfield, HD1 3DH, United Kingdom*
[4] Center for Nanophase Materials Sciences, *Oak Ridge National Laboratory, Oak Ridge, TN 37831, United States*
[5]*Department of Nuclear Engineering and Radiological Sciences, University of Michigan, Ann Arbor, MI 48109, United States*

Abstract

Grain growth and phase stability of a nanocrystalline face-centered cubic (fcc) $Ni_{0.2}Fe_{0.2}Co_{0.2}Cr_{0.2}Cu_{0.2}$ high-entropy alloy (HEA), either thermally- or irradiation-induced, are investigated through *in-situ* and post-irradiation transmission electron microscopy (TEM) characterization. Synchrotron and lab X-ray diffraction measurements are carried out to determine the microstructural evolution and phase stability with improved statistics. Under *in-situ* TEM observation, the fcc structure is stable at 300 °C with a small amount of grain growth from 15.8 to ~ 20 nm being observed after 1800 s. At 500 °C, however, some abnormal growth activities are observed after 1400 s, and secondary phases are formed. Under 3 MeV Ni room temperature ion irradiation up to an extreme dose of nearly 600 displacements per atom, the fcc phase is stable and the average grain size increases from 15.6 to 25.2 nm. Grain growth mechanisms driven by grain rotation, grain boundary curvature, and disorder are discussed.

Keywords: chemical disorder; ion-solid interactions; concentrated solid solution alloys

* Corresponding author: zhangy1@ornl.gov, Oak Ridge National Laboratory, Ph: 865-574-8518, Fax: 865-241-3650

1. Introduction

The continuous pursuit to develop metallic alloys has led to considerable increases in structural strength and improved functionality, as well as exciting research developments. Historically, the incorporation of alloying elements at low-concentrations has been widely used to achieve desired materials properties, such as improved creep-resistance, better yield strength, and significantly enhanced radiation performance. Many of today's structural alloys contain single or multiple phases with one principal element (e.g., Fe- or Ni-based alloys) or two dominant elements (e.g., (Fe-Cr)- or (Ni-Cr)-based alloys) modified by smaller additions of other elements. Most of these alloys, with the major elements acting as a solvent and the alloying elements as solutes, are termed dilute alloys. In dilute alloys, there is generally no solute-solute interaction; rather, solute neighbors are all solvent atoms. Adding solute elements in order to pin dislocations and impede their movement, therefore altering dislocation dynamics [1], has been a traditional approach for the enhancement of mechanical performance.

Continuous discoveries in the past 15 years of Concentrated Solid-solution Alloys (CSAs) with remarkable properties, unexpected from dilute alloys, have drawn immense attention and opened new frontiers in materials research. CSAs are composed of two to five (or more) elemental species, all at high concentrations. Unlike in dilute alloys, the principal elements in CSAs are randomly arranged on a simple crystalline lattice. These are generally simple face-centered cubic (fcc), body-centered cubic (bcc), or hexagonal closest packed (hcp) lattices, with few or none of the atoms having the same distribution of neighbors (i.e., the first and second nearest neighbors of constituents are different). The multi-component CSAs containing five or more elemental species, such as $Ni_{0.2}Fe_{0.2}Co_{0.2}Cr_{0.2}Cu_{0.2}$ (NiFeCoCrCu), are commonly termed high-entropy alloys (HEAs). The high chemical inhomogeneity feature is noteworthy for complex CSAs, including HEAs. In complex CSAs, compositional complexity can be achieved by modifying the number, type, and concentration of constituents. CSAs, having *3d* transition elements (from Cr to Cu) with similar atomic mass and size in a fcc structure, exhibit superior tensile strength and fracture toughness at both low and high temperatures [2-7], robust phase stability [8], ultrahigh low-temperature toughness [9], superparamagnetism [10], superconductivity [11], and two orders of

magnitude improvement in radiation tolerance [12]. New knowledge regarding concentrated alloys [2-17] has clearly revealed that compositional complexity (high chemical inhomogeneity), as opposed to the incorporation of dilute solutes [1], has a significant influence on defect dynamics that results in improved radiation performance [18-22].

Nanoscience and nanotechnology [23,24] with the ability to control individual atoms has led to many breakthroughs and applications. As the size of a structure reduces to a countable number of atoms, chemical, physical, electrical, optical and magnetic properties become fundamentally different from their bulk counterparts. Nanostructured materials [25-34], especially with grain sizes well below 100 nm, are of great academic and industrial interest, including uses such as novel catalysts, sensors, membranes, drug delivery, and advanced nuclear energy systems [25,35-38]. Research on improving radiation performance has been focused on engineering nanostructures in dilute alloys to increase sink density and strength (e.g., grain boundaries (GBs) and interfaces in pure metals or dilute alloys) or on incorporation of nanoscale features (precipitate/matrix interfaces) to mitigate displacement damage [3,30.31,36-42]. Although radiation-induced defects and defect clusters are expected to be trapped or eliminated in these chemical or structural inhomogeneities, interactions of defects with GBs, however, can lead to GB chemical and structural changes that involve further complications and pose additional scientific questions. Substitutional solid solutions, with increasing structural and chemical complexities that are intrinsic in HEAs, cause unique site-to-site distortion and a locally disordered chemical environment, which may have a profound effect on the fundamental processes determining defect dynamics [2-16,18-22]. Such extreme elemental inhomogeneities in HEAs may strongly affect microstructure evolution in nanocrystalline films under ion irradiation. While research has shown improved radiation resistance of some crystalline CSAs over traditional dilute alloys [18-22,43], the performance of nanocrystalline CSAs under ion irradiation is largely unknown. Nanocrystalline HEAs with atomic-level chemical inhomogeneity may offer additional possibilities to control defect migration and mass transport and thus may outperform more traditional nanocrystalline dilute alloys.

Unique properties of nanostructured materials depend on their structural integrity. Under radiation, a constant flux of defects moves towards and accumulates at the sinks (chemical or structural inhomogeneities), which may cause structural and compositional modifications and in turn, may modify the sink properties. Many nanomaterials suffer from microstructural coarsening (i.e., an inherent instability) attributed to thermally or irradiation-induced grain growth. Nuclear materials must perform in in extreme environments (e.g., the combination of radiation, high temperatures and compositional change over time) and require components to be intrinsically structurally stable. In this work, we study structural stability under thermal annealing (*equilibrium conditions*) and ion irradiation (*non-equilibrium conditions*) of nanocrystalline NiFeCoCrCu HEA films with a focus on both thermally-induced and irradiation-induced grain growth mechanisms.

2. Material and experimental procedure

2.1. Film deposition

The NiFeCoCrCu HEA films with thicknesses of ~70 nm and 1000 nm were sputter deposited on different substrates using a 50 mm diameter equiatomic composition target, fabricated from pure metals of Ni, Fe, Co, Cr, and Cu (>99.99%, weight percent). The deposition process was similar to that reported in Ref. 44, except a DC supply was used instead of an RF supply. The system was pumped to ~ 1×10^{-7} Torr before back-filling the system with an Ar flow rate of 25 sccm through a throttle valve setting to equilibrate the system at 5 mTorr. The target power was set to 200 W and pre-sputtered for 5 minutes with the shutter closed. The sputtering rate was 7 nm/min determined via cross section scanning electron microscope imaging. During the sputtering, no intentional substrate heating was applied. The thin and thick HEA films were deposited directly onto NaCl substrates and Si wafers, respectively. The 70 nm films were deposited on NaCl salt substrates (HEA/NaCl) to facilitate sample preparation procedures for *in-situ* annealing experiments within a transmission electron microscope (TEM), while the thick 1000 nm films deposited on Si (HEA/Si) were prepared for *ex-situ* ion irradiation studies.

2.2. Ni ion irradiation

The HEA/Si films were irradiated at room temperature (RT, 295 K) using 3 MeV Ni^{+} (self-ions) along the surface normal direction to 5 different fluences up to 2.35×10^{17} cm^{-2}, as listed in Table 1. The irradiations were carried out using the 3.0 MV tandem accelerator facility at the Ion Beam Materials Laboratory (IBML) located at the University of Tennessee campus [45]. A constant ion flux of 6.94×10^{12} $cm^{-2}s^{-1}$ was used for all implantations to minimize beam heating effects. Adjustable beam slits were used to define an irradiation area, and the ion beam was defocused and wobbled in the horizontal and vertical directions perform uniform irradiation. All samples were mounted on a molybdenum holder using double-sided carbon tape on the back of the samples.

The Stopping and Range of Ions in Matter code 2003 version (SRIM-2003) [46] in full-cascade mode was used to estimate the displacement damage, assuming a film density of 8.356 $g\cdot cm^{-3}$ (8.705×10^{22} $atoms\cdot cm^{-3}$) with a threshold displacement energy of 40 eV for all the constituent elements [47]. In order to compare ion and neutron irradiation results, the use of the quick Kinchin–Pease option in SRIM to compute radiation damage exposure has been recommended [48] within the nuclear community. This recommendation is simply based on less differences among the quick option, the MD results [49], and the NRT model [50,51]. Nevertheless, the authors also state [48] that (1) the MD results depend on the reliability of interatomic potentials used, (2) both SRIM and MD do not account for the charge state of the moving ions, (3) SRIM does not consider temperatures, and (4) the NRT model is chosen not for its accuracy, but for its broad adoption as a common standard for converting a calculable parameter. In this work, the displacement damage is estimated using the full-cascade mode, the SRIM prediction from the quick option is also included for easy conversion.

The theoretical density of a solid-solution alloy can be roughly estimated from the atomic fraction, atomic weight and density of each constituent element [52]. A recent experimental study of thermophysical properties has shown that the theoretical density and experimental value of a NiFeCoCrCu alloy were 8.324 and 8.295 $g\cdot cm^{-3}$ [17], respectively. The value of 8.356 $g\cdot cm^{-3}$ used in the simulation is the default value in SRIM. A slight change of this value does not induce noticeable

differences in predictions in Fig. 1 or affect conclusions in the current studiy. The damage profile estimated from SRIM is determined by the sum of the predicted vacancy concentrations using the column "Knock-Ons" from Ni ions and columns of "Vacancies" from target elements of Ni, Fe, Co, Cr and Cu (provided in VACANCY.txt), together with the replacement collisions (provided in NOVAC.txt) [53]. Assuming a bulk NiFeCoCrCu HEA, the predicted damage profile in displacements per atom (dpa) and the implanted Ni ion profile are shown in Fig. 1. The conversion factor from ion fluence (10^{14} cm^{-2}) to local dose (dpa) is indicated by a long-dashed line and a dotted-dashed line for the full-cascade and quick predictions, respectively. For a film of 1000 nm (indicated by the background shading), the average dose is taken at a depth of 500 nm as marked by a star. The peak dose (marked by a heart) under 3 MeV Ni irradiation is estimated to be located at 950 nm. In other words, the average and peak doses in the HEA films resulting from 10^{14} cm^{-2} Ni irradiation under full-cascade simulation are 0.1568 and 0.2522 dpa with injected Ni concentration at 0.00019% (a negligible level) and 0.0014%, as shown in Fig. 1. Given the 20% Ni in the HEA film and low concentration of the injected Ni ions, no injected self-ion effect is expected from the implanted Ni under the conditions in this study. For the five ion fluences, average doses ranging from 0.73 to 368.48 dpa are estimated, with the maximum peak dose approaching 600 dpa. Such a wide dose range is designed to evaluate the structural stability of nanocrystalline HEA under a prolonged extreme irradiation environment.

2.3. TEM characterization

The *in-situ* TEM characterization with video imaging was carried out to directly examine grain growth and microstructural evolution as a function of time at both 300 and 500 °C. These annealing experiments were performed in a Hitachi H-9500 TEM operating at 300 kV in the MIAMI-2 facility located at University of Huddersfield [54]. The vacuum in the Hitachi H-9500 TEM was 0.9 Torr. A Gatan double tilt heating holder was used for the annealing of nanocrystalline HEA films (~ 70 nm) that were placed on 500-mesh Mo grids. Images and videos were recorded using a Gatan OneView digital camera with 16 Mpx. The samples were heated in the temperature ramping mode up to 300 and 500 °C,

respectively, with a temperature ramp of 60 °C/min. When the desired temperature was reached, the samples were monitored *in situ* within the TEM in bright-field (BF) at a magnification of 120kx. The total annealing time of 30 minutes (1800 s) and 32 minutes 22 seconds (1942 s), comparable with the RT irradiation time (2160 s or 36 minutes, Table 1) of film-D, was used for the 300 and 500 °C thermal treatments. Selected area electron diffraction (SAED) was used to record diffraction patterns (camera length of 0.5 m) before and after the annealing experiments. A Gatan GIF Quantum SE camera was used to record unfiltered and zero-loss images of the samples before and after annealing, aiming at mapping the thickness of the samples.

Ex-situ post TEM examinations were conducted at the University of Michigan on Ni-irradiated samples, due to the long irradiation time (over 9 hours for the highest fluence) as shown in Table 1. The focused-ion beam (FIB) on a FEI Helios Nanolab workstation was used to prepare cross-sectional TEM and scanning transmission electron microscope (STEM) samples using FIB lift-out techniques [12]. Prior to characterization, the TEM foils were cleaned using a Fischione Plasma Cleaner to remove carbonaceous contamination. A double Cs-corrected JEOL 3100R05 STEM operated at 300 keV was employed for STEM-bright Field. The STEM images were taken with an inner angle of 59 mrad and camera length of 8 cm. Diffraction patterns were taken close to the irradiation surface using a selected area aperture with diameter of 50 μm.

2.4. Synchrotron and lab X-ray diffraction measurements

The thin films were collected from the HEA/NaCl samples and measured with synchrotron X-rays at the Cornell High Energy Synchrotron Source (CHESS) in a transmission geometry. The X-ray energy was 61.32 keV (λ=0.2022 Å), and beam size was 0.2×0.2 mm^2. The Bragg images were recorded using a two-dimensional image plate detector with pixel size of 200×200 μm^2. The diffraction image was then converted into diffraction profiles (Fig. 2) using Fit2D software [55]. All the instrumental parameters were calibrated using CeO_2 as the standard. The lattice parameters were derived from Rietveld refinement and grain size was estimated from the Williamson-Hall plot, shown as an inset in Fig. 2.

X-ray diffraction (XRD) measurements were also performed on the thick 1000 nm HEA/Si films using a PAnalytical X'pert Pro thin-film diffractometer at the Center for Nanophase Materials Sciences (CNMS) in the Oak Ridge National Laboratory (ORNL). The Cu $K_{\alpha 1}$ X-ray (λ=1.5406 Å) from a high-tension X-ray generator (45kV, 40A) was used. The sample orientation was optimized by scanning the sample along different axes. The results suggested that the as-deposited HEA/Si films were textured and only the strongest (111) Bragg peak can be detected with reasonable statistics. In order to obtain high intensity XRD profiles, the film samples were scanned by rotating around different axes. Scanning the incident angle of the X-ray beam suggested that the (111) peak had good intensity with an angle of 8-30˚. The incident beam was kept at θ=18˚ and a continuous 2θ scan was recorded with a step size of 0.01˚ for all the as-deposited and irradiated film samples (Table 2). The width of the columnar grains is estimated using the Scherrer formula from the (111) diffraction peak fitted with pseudo-Voigt functions, and summarized in Table 2.

3. Results

3.1 As-deposited nanocrystalline HEA films

The 70 nm HEA films measured with synchrotron X-rays at CHESS were a collection of free-standing films from the NaCl substrates. As shown in Fig. 2, a fcc single-phase structure with a lattice constant of 3.600(1) Å is identified. A method developed by Williamson and Hall [56,57] is applied to estimate the grain size. In this method, the average grain size (L) is determined using the equation $\beta\cdot\cos\theta = K\cdot\lambda/L + C\cdot\varepsilon\cdot\sin\theta$, where β is the full width at half maximum (FWHM) of Bragg peaks in radians, θ is the Bragg angle, λ (0.2022 Å) is the X-ray wavelength and ε is the microstrain. The parameters K and C are constants that depend on the shape of the grains. By fitting the individual Bragg diffraction peak with pseudo-Voigt functions, the Williamson-Hall plot of the thin film sample is shown as an insert in Fig. 2. The (200) diffraction has a big deviation from other peaks, an indication that the thin film has a long-range lattice distortion and is excluded from the linear fitting. The Williamson-Hall plot of $\beta\cdot\cos\theta$ versus $\sin\theta$, indicates that the strain ($C\cdot\varepsilon$) and size ($K\cdot\lambda/L$) components can be obtained from the slope and the

intercept, respectively. When taking the K and C values as 1 and 4 (commonly suggested [58-60]), respectively, the average grain size of 70 nm HEA films is estimated to be 9.3 (±2) nm and the microstrain is 0.006(1).

The microstructure analysis of the 70 nm NiFeCoCrCu HEA thin films is shown in Figs. 3-6. The grain size of the 70 nm films has a broad distribution. Checking different areas of the as-deposited films by TEM at room temperature, the average grain diameter, estimated from the area assuming a circular grain, is ~11 nm with a standard deviation of 6 nm. The large standard deviation is attributed to a few very small and large grains observed in a relatively limited number of grains that are sampled. Inspection of the bright-field TEM micrograph of the as-deposited film in Fig. 5(a), shows the presence of voided grain boundaries as is evidenced by the brighter contrast around GBs. This observation indicates that the grains have nucleated at low homologous temperatures into a columnar structure with tapered voids between columns, in agreement with zone I of the Movchan-Demichishin-Thornton (MDT) model of sputter-deposited coatings [61,62]. For the thick HEA/Si films, columnar grains are observed with increasing width (diameter) close to the surface, shown in Fig. 7 and Table 3.

All the as-deposited HEA/Si samples were also examined by XRD conducted around the (111) peak with a fixed incident angle. Experimental results have revealed that the HEA/Si films are strongly textured, and the strongest (111) Bragg peak is in good agreement with the SAED patterns taken during the ex-*situ* TEM characterization as shown in Fig. 8, as well as the *in-situ* TEM observation shown in Fig. 6. The average width of the long columnar grains of the as-deposited film is estimated to be ~ 15.6 nm with a standard deviation of 0.3 nm (Table 2). The XRD-determined width of 15.6 nm for the HEA/Si films (~ 1000 nm) is larger than the TEM-determined width of 9.3 nm for the HEA/NaCl films and 10.2 nm near the HEA/Si interface in Table 3. This is mainly attributed to the dense columnar microstructures at the early stage of film deposition as described by the MDT model [61] and supported by the columnar structure evolution along the deposition direction, as shown in Fig. 7.

It is worth mentioning that the apparent difference in grain size determined by XRD and TEM, easily noticeable in some cases discussed later, is attributed to the grain size variation, limited TEM

sampling, and location of the examination (distance to interface or surface). In this work, all samples were carefully labeled and examined both before and after thermal treatments or irradiation experiments. Nevertheless, XRD provides more representative results due to its significantly larger sampling region and the number of grains that are examined.

3.2 *In-situ* TEM observation of structural stability during thermal annealing

To evaluate the thermal stability, 70 nm nanocrystalline HEA films were used. These were floated off the NaCl substrates in distilled water and captured on Mo TEM grids. The annealing experiments were carried out in vacuum at 300 and 500 °C, respectively. Snapshots of the experiments taken from videos (see supplementary data online) are presented in Figs. 3 and 4 and show the morphological evolution of the nanocrystalline films. For the 300 °C thermal treatment, some microstructural changes, as marked by three pairs of ellipses in Figs. 3(a) and (b), are observed within the first ~ 3 minutes. Under prolonged annealing, up to 30 minutes, the microstructural images shown in Figs. 3(b)-(e) stay largely unchanged, suggesting both negligible grain activities and other microstructural changes. In other words, grain growth is basically inactive (except the initial growth within 3 minutes), and the nanocrystalline structure remains stable. Post-image analysis of the 300 °C annealed sample was performed from images taken from the video (see online supplementary data), where 50 grains with an average size of 15.8 (±6.0) nm at 0 s were followed. The size of 15.8 nm determined by TEM is larger than the 9.3 nm value which had been determined by synchrotron X-ray results. TEM, under the conditions in the current study, is not sensitive to very small grains (e. g., < 3 nm). In addition, grain growth has already taken off for nearly 5 minutes during the temperature ramp up from RT to 300 °C. During annealing after 163 s, the average grain size increases to 17.3 (±8.0) nm. A further increase of annealing time to 600 s at 300 °C leads to additional growth to ~ 20.0 (±7.6) nm, but no clear growth is detected during annealing from 600 to 1800 s.

During annealing at 500 °C, continuing grain activities (changes in contrast due to grain rotation and growth) and increase of grain size (i.e., average grain diameter) with increasing time are observed

throughout the experiment (32 m 22 s or 1942 s). In Figs. 4(a) and (b), images of the same region are chosen for comparison, while Figs. 4(c) to (f) are taken from a neighboring region. Growth kinetics are clearly observed, especially at the marked locations, for example those shown in the solid and dashed circles in Figs. 4(a) and (b), where the dark contrasted regions in (a) disappear in (b) after 110 s. Similarly, as marked by solid circles in Figs. 4(c) to (f), little contrast is observed in (c) after annealing for 306 s. However, a dark spot can be seen by 479 s and continues to develop up to 1423 s, and then the crystallite shrinks to nearly half of its size at 1942 s. Another growth activity is shown by the dashed circles, where small grains seen at 306 s develop into a large grain at 479 s (shown as a dark spot, ~ 12 nm) which then dissolves at 1423 and 1942 s. While the nanostructure is stable at 500 °C, some large crystallites reaching ~ 40 nm are observed (supplementary information, Fig. 1). In post-experiment image analysis, 50 gains with an average grain size of 20.8 (±8.3) nm (500 °C, after 1942 s), including two large grains of 1390.6 and 1511.6 nm^2, are observed. Assuming a circular shape, they have diameters of 42.1 and 43.9 nm, respectively. The sizes of these two grains were 13.9 and 14.4 nm at the start of the observation. Examining small grains ranging from 9.1 to 12 nm after 500 °C 1942 s annealing reveals that their initial size ranges from 8.8 to 12 nm at the beginning of annealing. These surprisingly stable small grains indicate that the overall grain growth may be at the expense of their neighbors with either much smaller grain size (not clearly observable) or grains with unstable GBs (high GB energy, less stable GB structures).

An overall summary is shown in Fig. 5 based on bright-field transmission electron microscopy (BFTEM) micrographs and spatial thickness maps, and in Fig. 6 based on SAED patterns of the as-deposited, 300 and 500 °C annealed films, respectively. Grain growth is prominently observed in the sample annealed at 500 °C as evident in Figs. 5(c) and (f), whereas insignificant differences are noted between the microstructure at RT and 300 °C, as shown in Figs. 5(a), (b), (d) and (e). The grain growth is clearly observed by analyzing the diffraction patterns taken after the annealing experiments, as shown in Fig. 6. The cubic structure of the film is indicated by the overlaid indices in Figs. 6(a)-(c). At RT and 300

°C, the SAED patterns consist only of polycrystalline Debye-Scherrer rings. For the sample annealed at 500 °C, clear crystalline spots are observed, indicating thermally-induced formation of relatively large crystallites. In addition, secondary phases appear, as clearly shown by the additional peaks in Fig. 6(d) for the 500 °C curve. Grain growth is also present in the EFTEM thickness map analysis in Figs. 5(d)-(f). A relatively smooth morphology is observed in Figs. 5(d) and (e). The rougher thickness distribution map in Fig. 5(f) for the 500 °C sample, as compared with the RT and 300 °C samples, is attributed to more elastic scattering.

3.3 Ion irradiation induced grain growth of 1000 nm nanocrystalline HEA/Si films

The microstructure of the as-deposited and ion irradiated HEA/Si films was characterized, and the corresponding BFTEM images and SAED patterns are shown in Figs. 7 and 8. Clearly columnar structure is observed in all the films. Moreover, the nanostructure is stable under the RT irradiations up to the highest fluence of 2.35×10^{17} cm^{-2}. Since the columnar grains have a narrower width close to the HEA/Si interface and become wider along the growth direction (close to the surface), the grain width is measured at four depths, 50 nm from the interface, and at 500, 300 and 50 nm from the film surface, respectively. The width of columnar grains is defined using a linear intercept method at different locations in ImageJ software. More than 3 measurements at each depth are conducted. The error is the standard deviation, ranging from 2 to 5.2 nm for columns 3-5. Considering the narrower width close to the interface, more than 5 measurements are performed to determine the average width, and the corresponding deviation is between 1 and 2.5 nm. The corresponding average width of columnar grains for both the as-deposited and irradiated films is summarized in Table 3. As shown in Fig. 8, the films consist of columnar grains with dense grain boundaries, faceted top surfaces, and an increased grain width. With continuing deposition (e.g., from 70 nm to 1000 nm), surface diffusion becomes the leading process and the film morphology transits from Zone I to Zone II. The increase of the width along deposition direction agrees well with the structure zone model for sputter deposition (i.e., MDT model) [61,62]. The SAED patterns in Fig. 8 are taken close to the irradiation surface with a large selected area aperture that includes ~half of the films

along the growth direction. The pattern in Fig. 8(a) shows a typical nanocrystalline structure for the as-deposited sample. The cubic phase is retained in all the irradiated films. Compared with the SAED patterns of the irradiated films, the more discrete diffraction spots are observed with increasing ion fluence, suggesting increased grain size and more aligned orientations.

The microstructure analysis is inherently limited in TEM and SAED due to an insufficient examined region (e.g., only several hundred nanometers in size). Aiming at achieving better statistics, XRD measurements conducted on both the as-deposited and irradiated HEA/Si films cover areas of several millimeters in size. As a much larger film area is characterized, the average grain size determined by XRD has better statistics and lower uncertainty than that characterized by TEM (resulting from much smaller number of examined grains). The fitted results from the XRD peaks are therefore used for grain size determination and general discussion of grain growth. Due to the strong texture of the films, only the (111) peak exhibits a reasonable intensity, as shown in Fig. 9. The grain diameter is estimated from Scherrer formula $L=K\lambda/(\beta_{hkl}\cdot\cos\theta)$, where λ (1.5406 Å) is the wavelength of X-ray, θ is the diffraction angle, β_{hkl} is the FWHM of the Bragg peak in radians after subtracting instrument broadening [57]. The K value is a dimensionless quantity depending on the shape of grains [58,59]. K = 0.89 has been suggested for spheres or particles, and values ranging from 0.83 to 0.91 for cubic structures (e.g., 0.94 for spherical crystals with cubic symmetry) [63]. In the absence of detailed shape information, K = 0.9 is expected to be a good approximation [58,59,64]. As observed by TEM (Fig. 7), the grains of the film have columnar shapes. Taking K=0.9 [58,59,64] for the current work, the estimated grain size (the average width of the columnar grains) of the unirradiated film ranges from 15.4 nm for Film-D and Film-F to 16.2 nm for Film-B, as listed in Table 2. Irradiation-induced grain growth is investigated using these pre-examined films. The FWHM of all the peaks becomes narrower with increasing average ion dose as marked, which clearly indicates the growth of the nanograins. The average size of the sequentially irradiated films and net growth under different ion fluences (doses) are also summarized in Table 2. Irradiations with ion

fluences ranging from 4.7×10^{14} cm^{-2} (0.73 dpa) to 2.4×10^{17} cm^{-2} (368.5 dpa) lead to an average grain growth from 2.6 to 9.8 nm for the lowest and highest fluences, respectively.

4. Discussion

4.1 Thermally-induced versus defect-simulated grain growth

One challenge of nanomaterial applications is the stability of grain size. Much research effort has been devoted towards understanding and controlling the grain growth of nanomaterials, including pining the grain boundaries [65-67,72] and lowering GB energies through solute segregation [68,69]. Temperature-dependent grain growth, either thermally-induced or defect-stimulated, has been reported [41,70-78]. Simulations reveal three grain-growth mechanisms, driven by grain rotation, curvature, and disorder [79-82], respectively. Both grain-rotation and curvature-driven growths are commonly observed during thermal treatments. The rotation–coalescence mechanism favors elimination of the smallest grains, removes the common GB between neighboring grains and results in the formation of highly elongated, unstable grains that then grow via the GB migration mechanism [79]. For curvature-driven GB migration, the motion of the high-energy (often high-mobility) GBs towards the center of their curvature leads to elimination or conversion of them into low-angle GBs and releases a large amount of energy [79,83,84].

Rapid disorder-driven grain growth under ion irradiation has also been observed experimentally [71-73] or revealed by molecular dynamics (MD) simulations [73]. When an ion moves through a solid, it undergoes many collisions and produces primary knock-on atoms (PKAs). Some high-energy recoils can create significant crystalline damage and lead to instability of the crystalline lattice through consecutive collision cascades and sub-cascades along the ion path. Grain growth under irradiation has been explained by the direct impact of displacement thermal spikes on GBs [85]. Within the displacement spikes, GBs migrate through atomic jumps that are biased by the local GB curvatures. MD simulations [73] have, however, revealed that irradiation-induced damage leads to unexpected fast grain growth due to the disorder-driven mechanism. MD simulations [73] show that the stochastic, non-uniform, localized damage processes play an important role in nanocrystalline grain growth. If irradiation-induced instability happens in small grains, the grains can be consumed by neighboring grains

having stable lattices (little or no irradiation-induced damage). If instability happens in a large grain, but close to a GB, the damaged part of the grain may be absorbed by the neighboring grain on the other side of the GB. At a simulation temperature of 2300 K for a model ceramic oxide (nanocrystalline ceria, a radiation tolerant material similar to the radiation tolerant HEA film), while a disordered grain disappears within 50 ps and neighboring grains grow, grain rotation and GB movements via the curvature-driven mechanism take a much longer time (e.g., 800 ps and 2500 ps, respectively) [73]. Disorder-driven grain growth is not limited to irradiation (*non-equilibrium conditions*). In fact, the disorder-driven grain growth can also be viewed as defect-stimulated growth that has been observed experimentally during both synthesis and under irradiation conditions [70-73,85]. Thermally-activated grain movement, especially at the beginning of high-temperature annealing, is also observed in nanocrystalline materials, due to the existence of high defect concentrations from synthesis.

Grain growth of nanocrystalline materials can be described by a power law expression $D^n - D_0^n = K_m\phi$, where D_0 is the initial mean grain diameter, ϕ is ion fluence, and K_m is proportional to the grain boundary mobility of the materials and the driving force [70,71,85]. Both n and K_m are constants that may be characteristic of the material system and the dominating grain growth mechanisms. It has been reported that, in pure metals, n=2 or 3 for thermally activated and irradiation-induced grain growth, respectively [85]. In nanocrystalline oxide films, n=5 or 6 for CeO_2 and 6 for ZrO_2 [70-73].

4.2 Thermally-induced growth of nanocrystalline NiFeCoCrCu thin HEA film

The *in situ* TEM annealing experiments have revealed that thermally-induced grain growth of nanocrystalline NiFeCoCrCu thin films has two major stages: (1) at RT and 300 °C, the fcc phase and nanocrystalline structure are observed to be stable with insignificant grain coarsening; and (2) at 500 °C, significant growth activities are observed with some abnormal grain growth that may relate to new phase formation.

Examining the recorded video images, changes in contrast are commonly observed, much more frequently at higher temperatures (500 °C) as discussed above. The loss of contrast between neighboring

grains is attributed to the consumption of the grains or disappearance of the boundary between two grains. To observe the contrast change, the orientation of neighboring grains must be within a few degrees, suggesting grain rotation to align with the same orientation and continued growth by GB migration via curvature-driven mechanism.

The bright-field micrographs in Figs. 5(a)-(c) show that a majority of the voided grain boundaries have vanished at 500 °C whereas they remain largely unchanged at 300 °C. This suggests that voided grain boundaries may act as a preferential diffusion path during the kinetics of grain growth. It is worth noting that TEM samples are only a few tens of nm thick. In the current *in-situ* TEM characterization, the thickness is ~70 nm. The two surfaces (originally the surface and the interface of the HEA/NaCl samples) would also act as strong defect sinks and may restrain the grain growth, therefore the corresponding thickness effects should not be neglected. At higher temperatures, defects can be thermally activated and their enhanced mobility along preferential diffusion paths towards defect sinks is expected to contribute significantly to the observed growth at 500 °C. This is consistent with the fact that the BFTEM contrast at voided grain boundaries decreases during annealing.

Some abnormal grain growth is observed, as shown in supplementary Fig. 1 in addition to SAED spots and peaks in Figs. 6(c) and (d). The abnormal grain growth may be related to the appearance of additional SAED spots, suggesting the formation of secondary phases. These results indicate that, after the initial thermodynamic equilibrium is reached (~ 300 s), the microstructure is driven towards a new stable state during the extended annealing to 1942 s.

4.3 Irradiation-induced growth of nanocrystalline NiFeCoCrCu HEA

When materials are bombarded with energetic particles during irradiation, defect evolution is considered to primarily involve atomic–level dynamics, where materials undergo structural damage and their properties degrade [1]. Accumulated radiation damage can modify the microstructure. Under ion irradiation, the temperature significantly affects defect dynamics and can have a large influence on the microstructural evolution. Five major temperature-dependent recovery stages in dilute alloys are

proposed in this work, based on research conducted over 70 years [86-89]. Stage I (~0.1 T_M, where T_M is the melting temperature) corresponds to the onset of long-range self-interstitial atom (SIA) migration. When the irradiation temperature is below Stage I, correlated (close-pair) or uncorrelated (long-range recombination of Frenkel defects from different primary displacement events) SIA migration is negligible. Stage II involves long-range migration of small SIA clusters and SIA-impurity complexes (i.e., mobile SIAs but immobile vacancies), and Stage III (~0.2 T_M) is associated with the onset of vacancy motion. Stage IV involves migration of vacancy and vacancy–impurity clusters (i.e., both SIAs and vacancies are mobile), and Stage V (~0.3 T_M) corresponds to thermal dissociation of sessile (displacement cascade-produced) vacancy clusters. Above Stage V, dislocation loop and network dislocation density monotonically decrease due to mobile defects and vacancy loop dissociation.

The melting temperature of NiFeCoCrCu HEA films can be estimated by averaging the solidus temperature and liquidus temperature of the material [90] or using the rule of mixture ($\Sigma X_i \cdot T^i_m$) where X_i and T^i_m are the molar fraction and melting temperature of the constituent element *i*, respectively [91]. In recent work [17], a Ni-Fe-Co-Cr-Cu fcc HEA was produced with a matrix phase formed by approximately 22at.% of Ni, Fe, Co, and Cr plus a reduced amount of ~11% Cu together with an embedded Cu-enriched (~67%) solid solution phase. The liquidus temperature of this alloy was determined to be 1382 °C (1655 K). Assuming that the T_M of the NiFeCoCrCu nanocrystalline HEA deposited in this work is close to 1650 K, room temperature irradiation is clearly below 0.2 T_M, and is thus likely to be between recovery Stages I and III. However, SIAs and small SIA clusters may be absorbed at GBs or remain mobile to recombine with sessile monovacancies and vacancy clusters.

In dilute alloys, suppression of nanocrystalline grain growth is commonly achieved through two mechanisms [42,92]: (1) kinetic stabilization by solute-drag effect to hinder GB mobility [65-67,93] or by pinning boundaries with a fine dispersion of precipitates [94]; and (2) thermodynamic stabilization by solute segregation to GBs in order to reduce the GB energy and to minimize or eliminate the driving force for growth [68,69]. In HEAs, high chemical inhomogeneity leads to lattice distortion, and therefore lattice

potential energy variation and higher activation energy along the diffusion path, and consequentially lower diffusion efficiency than that in dilute alloys. In other words, an atom would experience a fluctuating lattice potential energy due to different lattice distortions from its neighbors as well as coordination bonding along its diffusion path and accordingly a higher activation energy to overcome deep traps [6,90, 95-97]. Sluggish atomic-level diffusion and transport [95-97] has been experimentally observed to reduce elemental segregation and defect clustering [12,18,21], and is also anticipated to hinder grain growth under irradiation.

The ion-irradiation-induced grain growth determined from XRD measurements is summarized in Fig. 10. The power law fit suggests n=21 and K_m =1.5×10^{12}, which is significantly higher than n values in the literature. This difference is attributed to the more aggressive ion irradiation conditions and to sluggish defect dynamics [98]. Comparing the results from the 300 °C annealing in Fig. 11, the RT irradiation induces more rapid grain growth within the first 100 s, as suggested by the sharp curvature (i.e., the change in slope). While the ion flux may affect the curvature to some extent, MD simulations of radiation-resistant oxide materials [70-73] reveal that the observed swift process induced by disorder, as compared with the relatively slow grain rotation and GB migration mechanisms, is representative.

The sluggish diffusion arises from changes in defect energetics [15,99,100] due to the local chemical inhomogeneity and atomic-level segregation bias [98]. The sluggish diffusion in CSAs is theoretically investigated and explained by the difference in formation and migration energies of interstitial atoms in different CSAs. For example, higher migration barriers for interstitials and considerably reduced number of jumps (below the coordination number of the lattice in CSAs than those in pure Ni) are revealed, which lead to sluggish defect diffusion and small clusters. The diffusion mass transport in CSAs is not only slower than that in pure components but is also chemically biased [101]. While this study demonstrates the phase and microstructure stabilities under RT self-ion irradiation to nearly 600 dpa. Detailed comparison of irradiation responses of nanocrystalline HEAs versus

nanocrystalline dilute alloys requires systematic study over a wide range of temperatures and ion doses, beyond the scope of the current work.

5. Conclusion

The mechanisms of grain growth and the microstructural stability of nanocrystalline NiFeCoCrCu HEA films under both thermal annealing and ion irradiation are investigated. *In situ* TEM annealing experiments at 300 °C show that nanocrystalline grains grow starting from 15.8 (±6.0) nm to 17.3 (±8.0) nm at 163 s and then stabilize at ~20.0 (±7.6) nm, with no further growth detected from 600 to 1800 s and that the fcc phase is stable during the 300 °C annealing. At temperatures of 500 °C, significant grain growth occurs during the whole annealing period of 1942 s. In contrast with the observed microstructural stability under annealing at 300°C, secondary phases are formed at 500 °C. At low and moderate temperatures (≤300°C), while some defect atoms at GBs are expected to move into crystalline sites to reduce GB energies and small grains may be consumed by larger neighboring grains, the grain growth is significantly hindered by the suppressed kinetics (thermally inactive) of point defects characteristic of HEA systems. At higher temperatures (~ 500°C), the observed growth of nanocrystals is associated with the local reorganization of crystalline structures towards a different thermodynamic equilibrium state, conceivably with the nucleation of secondary phases, as manifested by differences in the *in situ* monitored diffraction patterns.

Radiation creates high concentrations of defects far beyond those found under thermal equilibrium conditions. During the interaction of energetic particles with HEAs, significant fluxes of point defects can be induced in the vicinity of GBs. In contrast with the *in-situ* annealing experiments within a TEM, the RT ion irradiation induces more rapid grain growth. The instant defect responses (at a *ps* timescale) and sequential migration (extending to μ*s* timescale or longer) effectively drive microstructural evolution via a disorder-driven mechanism. The grain size increases and follows an exponential law as a function of ion fluence or dpa, starting ~15.6 nm to 18.8, 21.0, 22.6, 23.9 and 25.2 nm at average doses of 0.73, 4.4, 23.5, 125.4 and 368.5 dpa. This leads to average grain growth from 2.6

to 9.8 nm at the lowest and highest fluences, respectively. The fcc phase is stable under the high-dose irradiation to nearly 600 dpa. The growth driven by irradiation-induced disorder (instability) is more rapid than the relatively slow grain rotation and GB migration mechanisms observed during annealing experiments.

Acknowledgments

This work was supported as part of the Energy Dissipation to Defect Evolution (EDDE), an Energy Frontier Research Center funded by the U.S. Department of Energy, Office of Science, Basic Energy Sciences under contract number DE-AC05-00OR22725. MAT was supported through the ASTRO fellowship, a United States Department of Energy workforce development program implemented at Oak Ridge National Laboratory through the Oak Ridge Institute for Science and Education under contract DE-AC05-06OR23100. The synchrotron X-ray measurement was conducted at the Cornell High Energy Synchrotron Source (CHESS), which is supported by the National Science Foundation under award DMR-1332208. The lab X-ray experiment was conducted at the Center for Nanophase Materials Sciences, which is a DOE Office of Science User Facility. The authors are grateful to the Engineering and Physical Sciences Research Council who funded MIAMI-2 under grant number EP/M028283/1. WLB is supported by the Chancellors Fellowship program at the University of Tennessee and by the National Science Foundation (CPS 1544686).

Appendix A. Supplementary data

Supplementary data to this article can be found online.

References

1. Was G S, 2017 Fundamentals of Radiation Materials Science: Metals and Alloys, Springer ISBN: 978–1–4939–3436–2 (Print) 978–1–4939–3438–6 (Online)
2. Li Z, Pradeep K G, Deng Y, Raabe D and Tasan C C 2016 Metastable high-entropy dual-phase alloys overcome the strength-ductility trade-off *Nature* **534** 227
3. Zou Y, Ma H and Spolenak R 2015 Ultra strong ductile and stable high-entropy alloys at small scales, *Nat. Commun.* **6** 7748
4 . Gludovatz B, Hohenwarter A, Catoor D, Chang E H, George E P and Ritchie R O 2014 A fracture-resistant high-entropy alloy for cryogenic applications *Science* **345** 1153
5. Gludovatz B, Hohenwarter A, Thurston K V S, Bei H, Wu Z, George E P and Ritchie R O 2016

Exceptional damage-tolerance of a medium-entropy alloy CrCoNi at cryogenic temperatures *Nat. Commun.* **7** 10602
6. Yeh J W, Chen S K, Lin S J, Gan J Y, Chin T S, Shun T T, Tsau C H and Chang S Y 2004 Nanostructured High-Entropy Alloys with Multiple Principal Elements: Novel Alloy Design Concepts and Outcomes *Adv. Eng. Mater.* **6** 299
7. Wei Y, Li Y, Zhu L, Liu Y, Lei X, Wang G, Wu Y, Mi Z, Liu J, Wang H and Gao H 2014 Evading the strength–ductility trade-off dilemma in steel through gradient hierarchical nanotwins *Nature Commun.* **5** 3580
8. Miracle D and Senkov O 2017 A critical review of high entropy alloys and related concepts *Acta Mater.* **122** 448-511
9. Diao H, Feng R, Dahmen K and Liaw P 2017 Fundamental deformation behavior in high-entropy alloys: an overview *Curr. Opin. Solid State Mater. Sci.*, **21** 252-266
10. Liu L, Zhu J B, Li J C and Jiang Q 2012 Microstructure and magnetic properties of $FeNiCuMnTiSn_x$ high entropy alloys *Adv. Eng. Mater.* **14** 919-922
11. Vrtnik S, Koželj P, Meden A, Maiti S, Steurer W, Feuerbacher M and Dolinšek J 2017 Superconductivity in thermally annealed Ta-Nb-Hf-Zr-Ti high-entropy alloys *J. Alloys Compd.* **695** 3530-3540
12. Lu C, Chen N, Niu L, Jin K, Yang T, Xiu P, Zhang Y, Gao F, Bei H, Shi S, He M R, Robertson I M, Weber W J and Wang L 2016 Enhancing radiation tolerance by controlling defect mobility and migration pathways in multicomponent single phase alloys *Nature Commun.* **7** 13564
13. Leino A A, Samoluyk G, Sachan R, Granberg F, Weber W J, Bei H, Lie J, Zhai P and Zhang Y 2018 GeV ion irradiation of NiFe and NiCo: insights from MD simulations and experiments *Acta Mater.* **151** 191
14. Sachan R, Ullah M W, Chisholm M F, Liu J, Zhai P, Schauries D, Kluth P, Trautman C, Bei H, Weber W J and Zhang Y 2018 Radiation-induced extreme elastic and inelastic interactions in concentrated solid solutions *Mater. Des.* **150** 1
15. Zhao S, Weber W J and Zhang Y 2017 Unique challenges for modeling defect dynamics in concentrated solid-solution alloys *JOM* **69** 2084
16. Zhao S, Egami T, Stocks G M and Zhang Y 2018 Effect of d electrons on defect properties in NiCoCr and NiCoFeCr concentrated solid solution alloys *Phys. Rev. Materials* **2** 013602
17. Wang W L, Meng L J, Li L H, Hu L, Zhou K, Kong Z H and Wei B B 2016 An Experimental Study of Thermophysical Properties for Quinary High-Entropy NiFeCoCrCu/Al Alloys *Chinese Phys. Lett.* **33** 116102
18. Zhang Y, Zhao S, Weber W J, Nordlund K, Granberg F and Djurabekova F 2017 Atomic-level heterogeneity and defect dynamics in concentrated solid-solution alloys *Curr. Opin. Solid State Mater. Sci.* **21** 221
19. Granberg F, Nordlund K, Ullah MW, Jin K, Lu C, Bei H, Wang L M, Djurabekova F, Weber W J and Zhang Y 2016 Mechanism of radiation damage reduction in equiatomic multicomponent single phase alloys *Phys. Rev. Lett.* **116** 135504
20. Zhang Y, Jin K. Xue H, Lu C, Olsen R J, Beland L K,. Ullah M W, Zhao S, Bei H, Aidhy D S, Samolyuk G D, Wang L, Caro M, Caro A, Stocks G M, Larson B C, Robertson I M, Correa A A and Weber W J 2016 Influence of Chemical Disorder on Energy Dissipation and Defect Evolution in Advanced Alloys *J. Mater. Res.* **31** 2363
21. Zhang Y, Stocks G M, Jin K, Lu C, Bei H, Sales B C, Wang L, Béland L K, Stoller R E, Samolyuk G D, Caro M, Caro A and Weber W J 2015 Influence of chemical disorder on energy dissipation and defect evolution in concentrated solid solution alloys *Nat. Commun.* **6** 8736
22. Velişa G, Wendler E, Zhao S, Jin K, Bei H, Weber W J and Zhang Y 2018 Delayed damage accumulation by athermal suppression of defect production in concentrated solid solution alloys *Mater. Res. Lett.* **6** 136

23. Moriarty P 2001 Nanostructured materials *Reports on Progress in Physics* **64** 297
24. Chookajorn T, Murdoch H A and Schuh C A 2012 Design of stable nanocrystalline alloys *Science* **337** 951
25. Beyerlein I J, Caro A, Demkowicz M J, Mara N A, Misra A and Uberuaga B P 2013 Radiation damage tolerant nanomaterials *Materials Today* **16** 443
26. Norris D J, Efros A L and Erwin S C, 2008 Doped Nanocrystals *Science* **319** 1776
27. Fan H, Yang K, Boye D M, Sigmon T, Malloy K J, Xu H, López G P and Brinker C J 2004 Self-assembly of ordered, robust, three-dimensional gold nanocrystal/silica arrays *Science* **304** 567
28. Kovalenko M V, Scheele M and Talapin D V 2009 *Science* **324** 1417
29. Sun C, Lia H and Chen L, 2012 *Energy Environ. Sci.* **5**, 8475
30. Jiang S, Wang H, Wu Y, Liu X, Chen H, Yao M, Gault B, Ponge D, Raabe D, Hirata A, Chen M, Wang Y and Lu Z 2017 Ultrastrong steel via minimal lattice misfit and high-density nanoprecipitation *Nature* **544** 460–464
31. Yang T, Zhao Y L, Tong Y, Jiao Z B, Wei J, Cai J X, Han X.D, Chen D, Hu A, Kai J J, Lu K, Liu Y and Liu C T 2018 Multicomponent intermetallic nanoparticles and superb mechanical behaviors of complex alloys *Science* **362** 933–937
32. Du C, Jin S, Fang Y, Li J, Hu S, Yang T, Zhang Y, Huang J, Sha G, Wang Y, Shang Z, Zhang X, Sun B, Xin S and Shen T 2018 Ultrastrong nanocrystalline steel with exceptional thermal stability and radiation tolerance *Nat. Commun.* **9** 5389
33. Si S, Li W, Zhao X, Han M, Yue Y, Wu W, Guo S, Zhang X, Dai Z, Wang X, Xiao X and Jiang C 2017 Significant Radiation Tolerance and Moderate Reduction in Thermal Transport of a Tungsten Nanofilm by Inserting Monolayer Graphene *Adv. Mater.* **29** 1604623
34. Li Z and Chen F 2017 Ion beam modification of two-dimensional materials: Characterization, properties, and applications *Appl. Phys. Rev.* **4** 011103
35. Zinkle S J and Snead L L 2014 Designing radiation resistance in materials for fusion energy *Ann. Rev. Mater. Res.* **44** 241
36. Wurster S and Pippan R 2009 Nanostructured metals under irradiation *Scr. Mater.* **60** 1083
37. Demkowicz M J, Bellon P and Wirth B D 2010 Atomic-scale design of radiation-tolerant nanocomposites *MRS Bulletin* **35** 992
38. Schuster B E, Ligda J P, Pan Z L and Wei Q 2011 Nanocrystalline refractory metals for extreme condition applications *JOM* **63** 27
39. El-Atwani O, Nathaniel J E, Leff A C, Hattar K and Taheri M L 2017 Direct observation of sink-dependent defect evolution in nanocrystalline iron under irradiation *Sci. Rep.* **7** 1836
40. Han W, Demkowicz M J, Mara N A, Fu E, Sinha S, Rollett A D, Wang Y, Carpenter J S, Beyerlein I J and Misra A 2013 Design of radiation tolerant materials via interface engineering *Adv. Mater.* **25** 6975
41. Kotan H, Darling K A, Saber M, Scattergood R O and Koch C C 2013 An *in situ* experimental study of grain growth in a nanocrystalline $Fe_{91}Ni_8Zr_1$ alloy *J Mater Sci* **48** 2251
42. Koch C C, Scattergood R O, Saber M and Kotan H 2013 High temperature stabilization of nanocrystalline grain size: Thermodynamic versus kinetic strategies *J. Mater. Res.* **28** 1785
43. Nagasse T, Rack P D, Noh J H and Egami T 2015 In-situ TEM observation of structural changes in nano-crystalline CoCrCuFeNi multicomponent high-entropy alloy (HEA) induced under fast electron irradiation by high voltage electron microscopy (HVEM) *Intermetallics* **59** 32
44. An Z, Jia H, Wu Y, Rack P D, Patchen A D, Liu Y, Ren Y, Li N and Liaw P K 2015 Solid-Solution CrCoCuFeNi High-Entropy Alloy Thin Films Synthesized by Sputter Deposition *Mater. Res. Lett.*, **3** 203
45. Zhang Y, Crespillo M L, Xue H, Jin K, Chen C H, Fontana C L, Graham J T and Weber W J 2014 New ion beam materials laboratory for materials modification and irradiation effects research *Nucl. Instrum. Methods Phys. Res. B* **338** 19

46. Ziegler J F, Ziegler M D and Biersack J P 2010 SRIM – The stopping and range of ions in matter *Nucl. Instrum. Methods Phys. Res. B* **268** 1818
47. ASTM E521, Standard Practice for Neutron Radiation Damage Simulation by Charged-Particle Irradiation, Annual Book of ASTM Standards, Vol. 12.02, ASTM International, West Conshohocken, PA, 2009
48. Stoller R E, Toloczko M B, Was G S, Certain A G, Dwaraknath S and Garner F A 2013 On the use of SRIM for computing radiation damage exposure *Nucl. Instrum. Methods Phys. Res. B* **310** 75
49. Nordlund K, Zinkle S J, Sand A E, Granberg F, Averback R S, Stoller R, Suzudo T, Malerba L, Banhart F, Weber W J, Willaime F, Dudarev S L and Simeone D 2018 Improving atomic displacement and replacement calculations with physically realistic damage models *Nature Comm.* **9** 1084
50. Norgett M J, Robinson M T and Torrens I M 1975 A proposed method of calculating displacement dose rates *Nucl. Eng. Des*. **33** 50
51. Robinson M T and Torrens I M 1974 Computer simulation of atomic-displacement cascades in solids in the binary-collision approximation *Phys. Rev. B* **9** 5008
52. Senkov O N, Wilks G B, Miracle D B, Chuang C P and Liaw P K 2010 Refractory high-entropy alloys *Intermetallics* **18** 1758
53. Zhang Y, Lian J, Zhu Z, Bennett W D, Saraf L V, Rausch J L, Hendricks C A, Ewing R C and Weber W J 2009 Response of strontium titanate to ion and electron irradiation *J. Nucl. Mater.* **389** 303
54. Harrison R W, Hinks, J A and Donnelly S E 2018 Influence of pre-implanted helium on dislocation loop type in tungsten under self-ion irradiation *Scripta Materialia* **150** 61
55. Hammersley A P, Svensson S O and Thompson A 1994 Calibration and correction of spatial distortions in 2D detector systems *Nucl. Instr. Meth.*, A **346** 312
56. Williamson G K and Hall W H 1953 X-ray line broadening from filed aluminum and wolfram *Acta Metall.* **1** 22
57. Scherrer P, 1918 Bestimmung der Grösse und der inneren Struktur von Kolloidteilchen mittels Röntgenstrahlen, Nachrichten von der Gesellschaft der Wissenschaften, Gottingen *Nachrichten Math. Phys.* **2** 98
58. Klug H P and Alexander L E 1974 X-Ray Diffraction Procedures 2nd edn, Ch. 9 (Wiley, 1974)
59. Holzwarth U and Gibson N 2011 The Scherrer equation versus the Debye-Scherrer equation *Nature Nanotechnology* **6** 534
60. Kristallogr Z, Leineweber A and Mittemeijer E J 2006 Anisotropic microstrain broadening due to compositional inhomogeneities and its parametrization *Suppl.* **23** 117
61. Thornton J A 1974 Influence of apparatus geometry and deposition conditions on the structure and topography of thick sputtered coatings *J. Vac. Sci. Technol. A* **11** 666
62. Mukherjee S and Gall D 2013 Structure zone model for extreme shadowing conditions *Thin Solid Films* **527** 158
63. Langford J I and Wilson A J C 1978 Scherrer after sixty years: A survey and some new results in the determination of crystallite size *J. Appl. Cryst.* **11** 102
64. Cullity B D 1978 *Elements of X-ray Diffraction* 2nd edn (Addison-Wesley, 1978)
65. Michels A, Krill CE, Ehrhardt H, Birringer R and Wu D T 1999 Modeling the influence of grain-size-dependent solute drag on the kinetics of grain growth in nanocrystalline materials *Acta Mater.* **47** 2143
66. Dey S, Mardinly J, Wang Y, Valdez J A, Holesinger T G, Uberuaga B P, Ditto J J, Drazina J W and Castro R H R 2016 Irradiation-induced grain growth and defect evolution in nanocrystalline zirconia with doped grain boundaries *Phys. Chem. Chem. Phys.* **18** 16921
67. Donaldson O K, Hattar K, Kaub T and Thompson G B 2018 Solute stabilization of nanocrystalline tungsten against abnormal grain growth *J. Mater. Res.* **33** 68
68. Kirchheim R 2002 Grain coarsening inhibited by solute segregation *Acta Mater.* **50** 413

69. Kirchheim R 2007 Reducing grain boundary, dislocation line and vacancy formation energies by solute segregation. I. Theoretical background *Acta Mater.* **55** 5129
70. Zhang Y, Aidhy D S, Varga T, Moll S, Edmondson P D, Namavar F, Jin K, Ostrouchov C N and Weber W J 2014 The effect of electronic energy loss on irradiation induced grain growth in nanocrystalline oxides *Phys. Chem. Chem. Phys.* **16** 8051
71. Zhang Y, Edmondson P D, Varga T, Moll S, Namavar F, Lan C and Weber W J 2011 Structural Modification of Nanocrystalline Ceria by Ion Beams *Phys. Chem. Chem. Phys.* **13** 11946
72. Zhang Y, Jiang W, Wang C, Namavar F, Edmondson P D, Zhu Z, Gao F, Lian J and Weber W J 2010 Grain growth and phase stability of nanocrystalline cubic zirconia under ion irradiation *Phys. Rev. B* **82** 184105
73. Aidhy D S, Zhang Y and Weber W J 2014 A fast grain-growth mechanism revealed in nanocrystalline ceramic oxides *Scripta Materialia* **83** 9
74. Aidhy D S, Zhang Y and Weber W J 2013 Stabilizing nanocrystalline grains in ceramic-oxides *Phys. Chem. Chem. Phys.* **15** 18915
75. Simões S, Calinas R, Vieira M T, Vieira M F and Ferreira1 P J 2010 In situ TEM study of grain growth in nanocrystalline copper thin films *Nanotechnology* **21** 145701
76. Bufford D C, Abdeljawad F F, Foiles S M and Hattar K 2015 Unraveling irradiation induced grain growth with in situ transmission electron microscopy and coordinated modeling *Appl. Phys. Lett.* **107** 191901
77. Liu W B, Zhang C, Ji Y Z, Yang Z G, Zang H, Shen T L and Chen L Q 2014 Irradiation-induced grain growth in nanocrystalline reduced activation ferrite/martensite steel *Appl. Phys. Lett.* **105** 121905
78. Voegeli W, Able K and Hahn H 2003 Simulation of grain growth in nanocrystalline nickel induced by ion irradiation *Nucl. Instr. Meth.*, **202** 230
79. Haslam A J, Moldovan D, Phillpot S R, Wolf D and Gleiter H 2002 Combined Atomistic and Mesoscale simulation of grain growth in nanocrystalline thin films *Comp. Mat. Sci.* **23** 15
80. Moldovan D, Yamakov V, Wolf D and Phillpot S R 2002 Scaling Behavior of Grain-Rotation-Induced Grain Growth *Phys. Rev. Lett.* **89** 206101
81. Atkinson H V 1988 Theories of normal grain growth in pure single phase systems *Acta Metall.* **36** 469
82. Humphreys F J and Hatherly M 1998 Recrystallization and Related Annealing Phenomena, Pergamon Press, Oxford, 1995; in: H. Weiland, B.L. Adams, A.D Rollett (Eds.), Grain Growth in Polycrystalline Materials III, TMS Publishing, Warrendale, PA
83. Moore L J, Dear R D, Summers M D, Dullens R P and Ritchie G A 2010 Direct observation of grain rotation-induced grain coalescence in two-dimensional colloidal crystals *Nano Lett.* **10** 4266
84. Harris K E, Singh V V and King A H 1998 Grain Rotation in Thin Films of Gold *Acta Mater.* **46** 2623
85. Kaoumi D, Motta A T and Birtcher R C 2008 A thermal spike model of grain growth under irradiation *J. Appl. Phys.* **104** 073525
86. Wigner E P 1946 Theoretical Physics in the Metallurgical Laboratory of Chicago *J. Appl. Phys.* **17** 857
87. Iwata T and Iwase A 1990 Damage Production and Annealing in Ion-Irradiated Fcc Metals *Radiation Effects and Defects in Solids* **113** 135
88. Zinkle S J and Singh B N 1993 Analysis of displacement damage and defect production under cascade damage conditions *J. Nucl. Mater.* **199** 173
89. Zinkle S J 2012 Chapter: Radiation-Induced Effects on Microstructure, In book: Comprehensive Nuclear Materials, vol. 1, Chapter: 1.03, Publisher: Elsevier, Editors: R. Konings 65-98

90. Cheng C-Y, Yang Y-C, Zhong Y-Z, Chen Y-Y, Hsu T and Yeh J-W 2017 Physical metallurgy of concentrated solid solutions from low-entropy to high-entropy alloys *Curr. Opin. Solid State Mater. Sci.* **21** 299
91. Yang X and Zhang Y 2012 Prediction of high-entropy stabilized solid-solution in multicomponent alloys *Mater. Chem. Phys.* **132** 233
92. Koch C C, Scattergood R O, Darling K A and Semones J E 2008 Stabilization of nanocrystalline grain sizes by solute additions *J. Mater. Sci.* **43** 7264
93. Cahn J W 1962 Impurity-drag effect in grain boundary motion *Acta Metal.* **10** 789
94. Nes E, Ryum N and Hunderi O 1985 On the Zener drag *Acta Metal.* **33** 11
95. Tsai K-Y, Tsai M-H and Yeh J-W 2013 Sluggish diffusion in Co–Cr–Fe–Mn–Ni high entropy alloys *Acta Mater.* **61** 4887
96. Dąbrowa J, Kucza W, Cieślak G, Kulik T, Danielewski M and Yeh J-W 2016 Interdiffusion in the FCC-structured Al-Co-Cr-Fe-Ni high entropy alloys: Experimental studies and numerical simulations *J. Alloys Comp.* **674** 455
97. Tsai M-H and Yeh J-W 2014 High-entropy alloys: a critical review *Mater. Res. Lett.* **2** 107
98. Osetsky Y N, Béland L K, Barashev A V and Zhang Y 2018 On the existence and origin of sluggish diffusion in chemically disordered concentrated alloys *Curr. Opin. Solid State Mater. Sci.* **22** 64
99. Zhao S, Stocks G M and Zhang Y 2016 Defect energetics of concentrated solid-solution alloys from ab initio calculations: $Ni_{0.5}Co_{0.5}$, $Ni_{0.5}Fe_{0.5}$, $Ni_{0.8}Fe_{0.2}$ and $Ni_{0.8}Cr_{0.2}$ *Phys. Chem. Chem. Phys.* **18** 24043
100. Zhao S, Osetsky Y N and Zhang Y 2017 Preferential diffusion in concentrated solid solution alloys: NiFe, NiCo and NiCoCr *Acta Mater.* **128** 391
101. Barashev A, Osetsky Y, Bei H, Lu C, Wang L and Zhang Y 2019 Chemically-biased diffusion and segregation impede void growth in irradiated Ni-Fe alloys *Curr. Opin. Solid State Mater. Sci.* https://doi.org/10.1016/j.cossms.2018.12.001

Table 1. Irradiation conditions of 3 MeV Ni irradiation of the HEA/Si films to different fluences, together with the average dose and peak dose (dpa) as predicted by full-cascade and quick SRIM simulations, respectively.

Sample	Fluence (cm^{-2})	Time	Average dose (dpa)		Peak dose (dpa)	
			Full cascade	Quick	Full cascade	Quick
Film-A	0	0	0	0	0	0
Film-B	4.7×10^{14}	1 m 7s	0.7	0.3	1.2	0.5
Film-C	2.8×10^{15}	6 m 43 s	4.4	1.9	7.1	3.0
Film-D	1.5×10^{16}	36 m	23.5	10.2	37.8	16.0
Film-E	8.0×10^{16}	3 h 12 m	125.4	54.2	201.8	85.3
Film-F	2.4×10^{17}	9 h 23 m 59 s	368.5	159.1	592.7	250.5

Table 2. Diffraction angle (θ), full width at half maximum (β) of the (111) Bragg peak, and the estimated grain size (L) from the XRD measurements before and after Ni irradiation of the HEA/Si samples. The corresponding standard deviation is listed in parentheses. The grain growth is shown in the last column. The standard deviation of the FWHM is 0.3 nm.

sample	**As-deposited**			**After irradiation**			**Growth**
	2θ (°)	**FWHM (°)**	**L (nm)**	**2θ**	**FWHM**	***L* (nm)**	**ΔL (nm)**
Film-B	43.654(2)	0.529(6)	16.2	43.690(2)	0.456(5)	18.8	2.6
Film-C	43.654(2)	0.551(1)	15.5	43.628(1)	0.408(4)	21.0	5.5
Film-D	43.642(1)	0.554(4)	15.4	43.651(1)	0.379(3)	22.6	7.2
Film-E	43.631(2)	0.550(6)	15.6	43.570(1)	0.358(1)	23.9	8.3
Film-F	43.633(2)	0.555(7)	15.4	43.553(1)	0.339(2)	25.2	9.8

Table 3. The average width (nm) of the columnar grains in HEA/Si films, irradiated to the different fluences described in Table 1. Four different locations were measured: at ~50 nm from the HEA and Si substrate interface, and at 500, 300 and 50 nm to the film surface, respectively. The standard deviation is up to 2.5 nm and 5.2 nm for column 2 and columns 3-5, respectively.

sample	**50 nm to interface**	**500 nm to Surface**	**300 nm to surface**	**50 nm to surface**
Film-A	10.2	9.8	11.8	14.6
Film-B	11.0	30.4	34.1	40.0
Film-C	11.9	30.9	39.5	40.5
Film-D	12.2	36.9	40.9	43.8
Film-E	12.6	38.2	47.2	46.9
Film-F	14.7	52.6	66.9	67.7

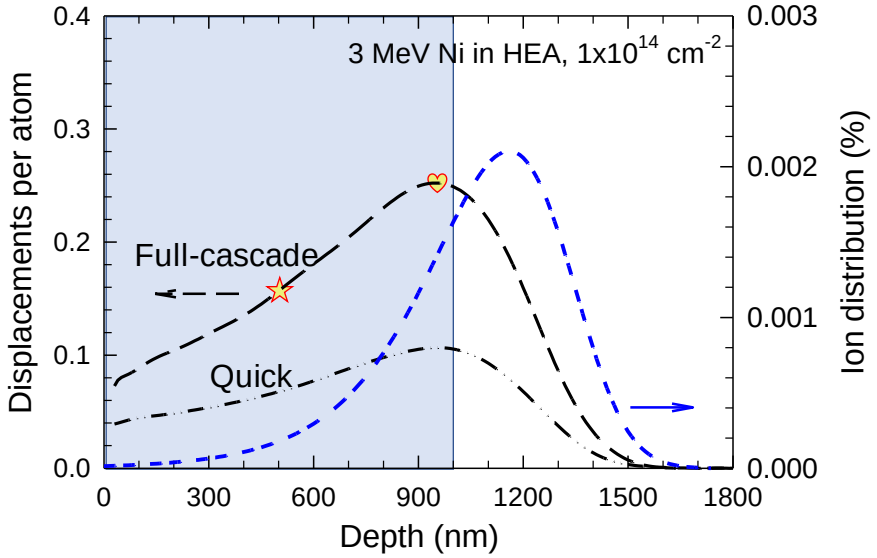

FIG. 1. SRIM predicted damage profile (left axis) predicted from both full-cascade and quick option, together with implanted Ni concentration (right axis) under 3 MeV Ni irradiation to an ion fluence of 1×10^{14} cm^{-2}. The film thickness of 1000 nm is shown as a shaded area in the background.

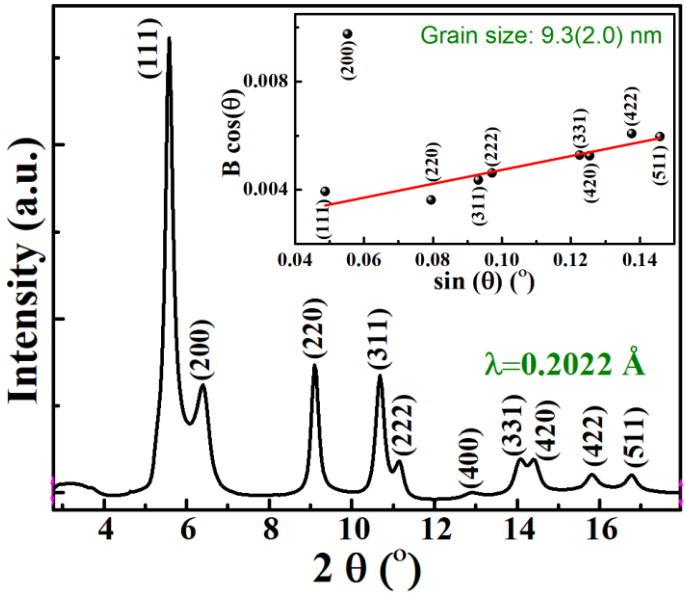

FIG. 2. High-energy synchrotron XRD measurement of a stack of free standing thin NiFeCoCrCu HEA films (70 nm) taken from the NaCl substrates, showing the fcc structure. The inset is the W-H plot indicating the grain size of 9.3 (±2) nm.

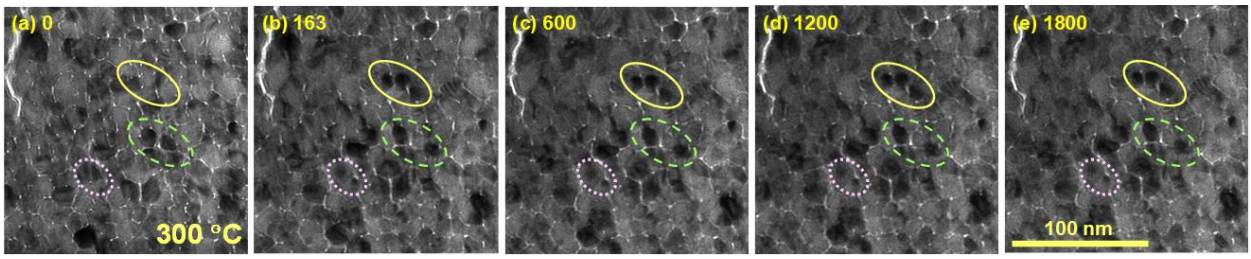

FIG. 3. Thermal evolution of a thin nanocrystalline HEA film annealed at 300 °C for 1800 s. All micrographs are taken at the same magnification with the scale bar shown in (e) and the elapsed time marked on each micrograph. For better comparison of thermally-induced activities, the same locations are marked on each micrograph by ellipses. The video can be found online in the supplementary data.

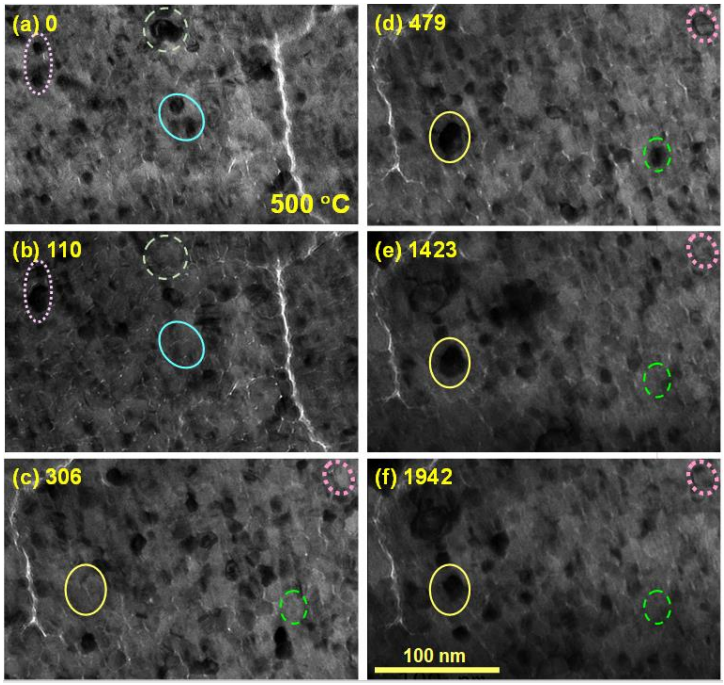

FIG. 4 Thermal evolution of a thin nanocrystalline HEA film annealed at 500 °C for 1942 s. All micrographs are taken at the same magnification with the scale bar shown in (f) and the elapsed time marked on each micrograph. For better comparison of thermally-induced structural changes, the same locations are marked on each micrograph by ellipses. The video can be found online in the supplementary data.

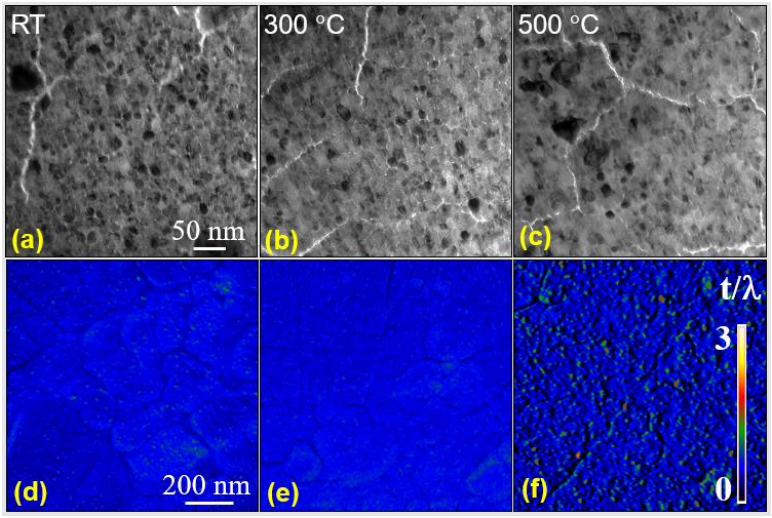

FIG. 5. (a-c) BFTEM images and(d-f) thickness map of the 70 nm nanocrystalline HEA films at RT (left), 300 °C (middle) and 500°C (right) samples. The scale bars in (a) and (d) also apply to the images in the same row.

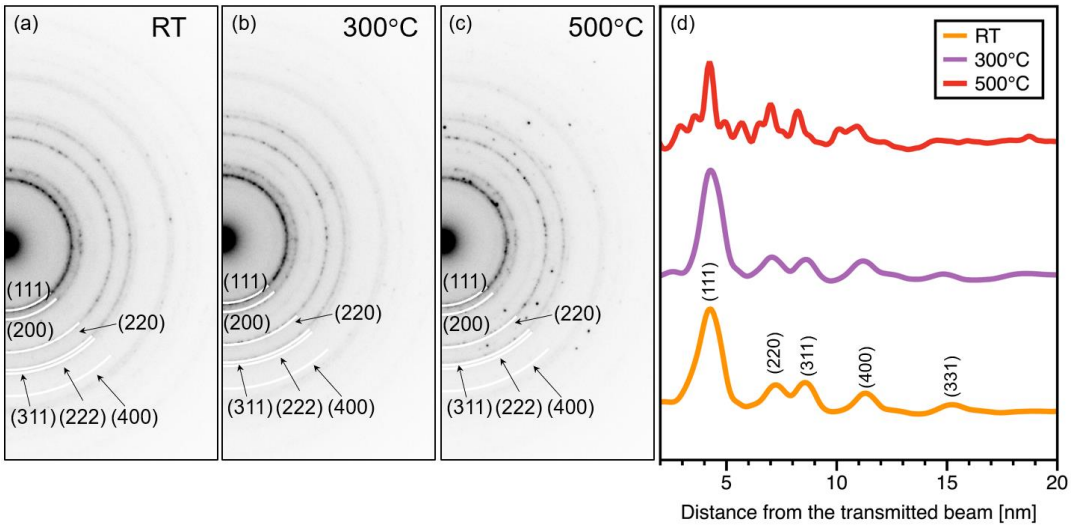

FIG. 6. Diffraction patterns with overlaid indices of the 70 nm nanocrystalline HEA films at (a) RT, (b) 300°C after 1800 s annealing and (c) 500°C after 1942 s annealing, together with (d) their intensity plot. The crystallographic indices are labelled accordingly and agree well with the results from the synchrotron XRD patterns shown in Fig. 2.

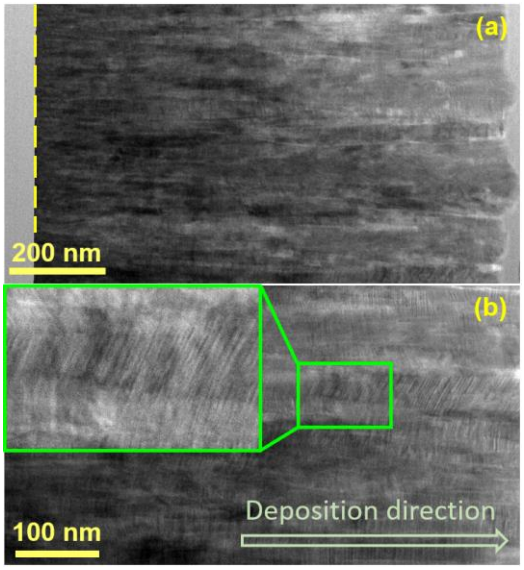

FIG. 7. (a) Cross-sectional TEM micrograph of the as-deposited thick HEA film (~1000 nm) on Si substrate, and (b) higher magnification image showing the highly textured columnar grain structure along the deposition direction (along the surface normal as shown by the arrow). The vertical dashed line in (a) indicates the interface of the HEA film and the substrate. The inset in (b) shows the grain structure and GB quality.

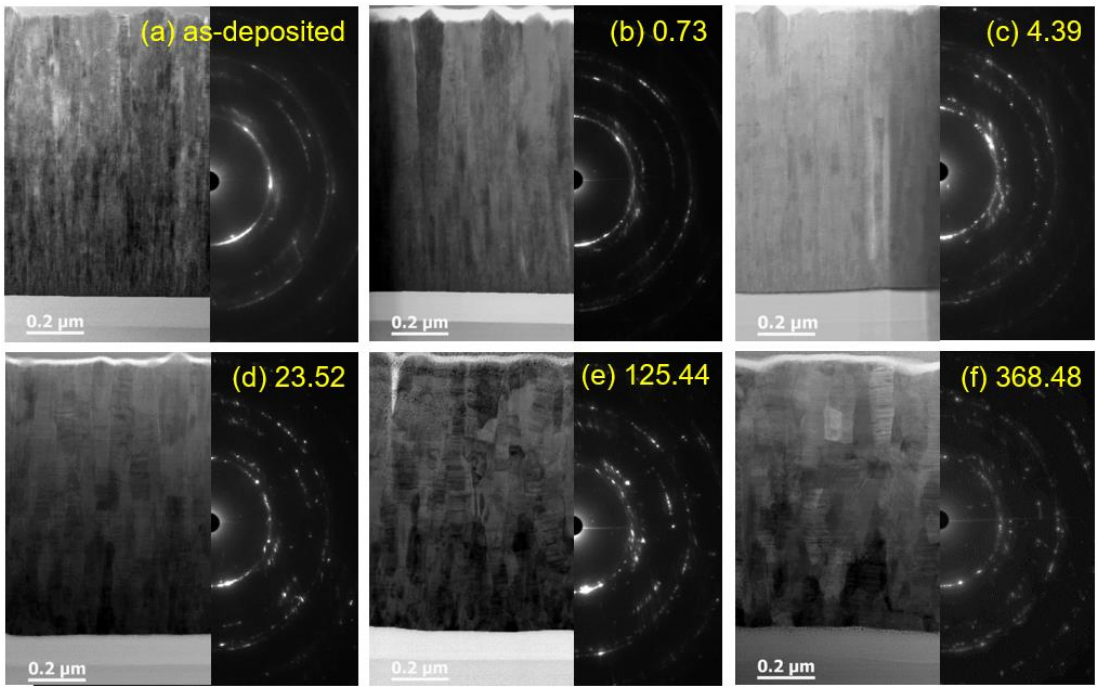

FIG. 8. TEM micrographs of as-deposited and irradiated HEA/Si films with increasing irradiation dose, at approximately 500 nm from the film surface, as noted on the corresponding images. The average doses range from (b) 0.73 dpa to (f) 368.5 dpa. The corresponding SAED patterns are shown on the right-hand side.

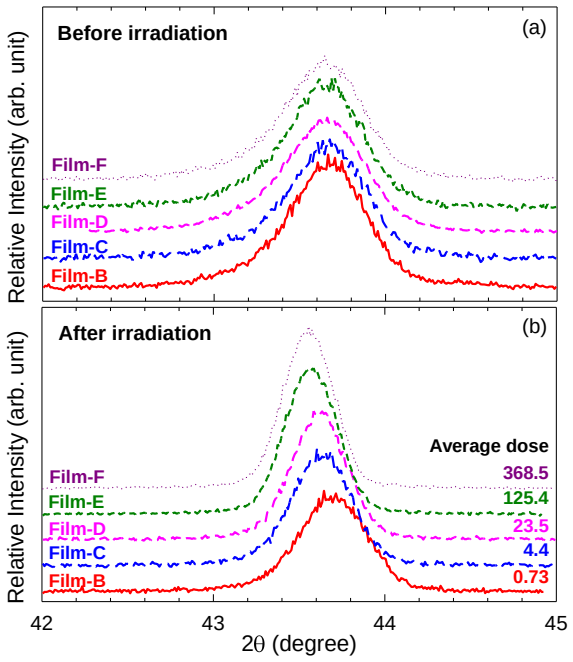

FIG. 9. XRD spectra of (a) the as-deposited HEA films and (b) the films irradiated at room temperature to different fluences (Table 1). The average irradiation doses are marked on the plot.

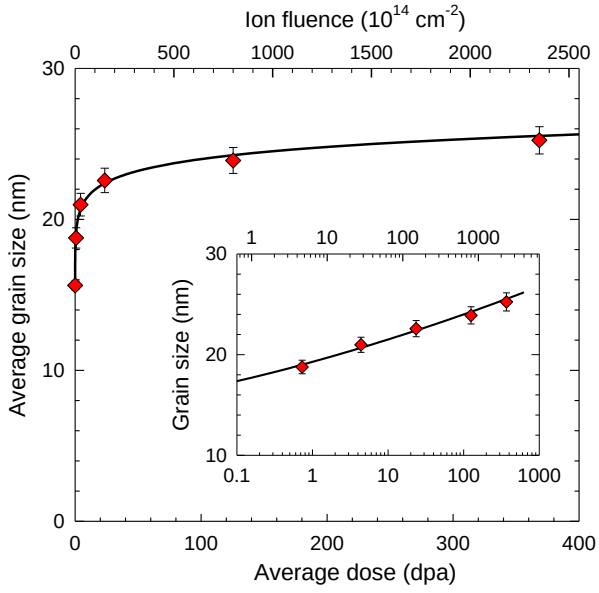

FIG. 10. Irradiation-induced grain growth as a function of either average dose (bottom axis) or ion fluence (top axis). The uncertainty of the grain size is indicated by error bars. The solid line is the model fit to a power law expression with n=21 and K_m=1.5×10^{12}.

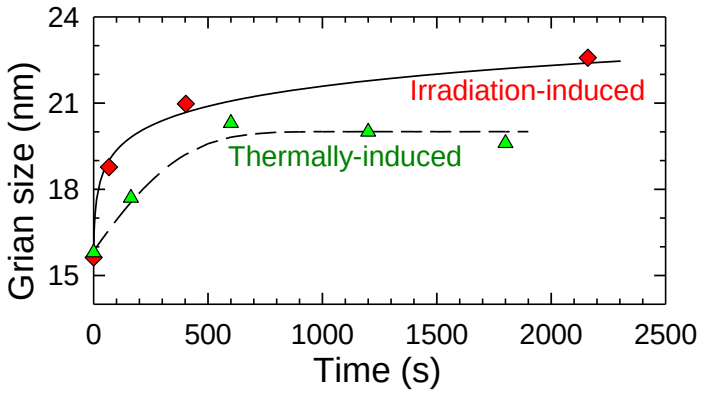

FIG. 11. Comparison of grain growth as a function of time under room temperature irradiation and thermal annealing at 300 °C. The solid line is the model fit, and the dashed line is a smooth fit to guide the eye.

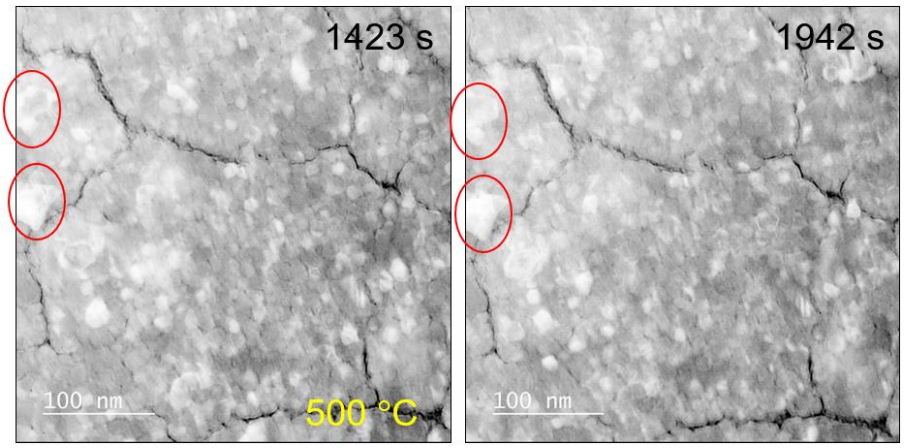

Supplementary Fig. 1 Inverse contrast BFTEM micrographs of the 70 nm nanocrystalline HEA film thermally treated at 500 °C to 1423 and 1942 s. Some large crystallites with dimensions of ~ 40 nm are observable, as marked.